Internal Porosity of Mineral Coating Supports Microbial Activity in Rapid Sand Filters for Groundwater Treatment

Gülay, Arda; Tatari, Karolina; Musovic, Sanin; Mateiu, Ramona Valentina; Albrechtsen, Hans-Jørgen; Smets, Barth F.

Published in:
Applied and Environmental Microbiology

Link to article, DOI:
10.1128/AEM.01959-14

Publication date:
2014

Document Version
Publisher's PDF, also known as Version of record

Applied and Environmental Microbiology

Internal Porosity of Mineral Coating Supports Microbial Activity in Rapid Sand Filters for Groundwater Treatment

Arda Gülay, Karolina Tatari, Sanin Musovic, Ramona V. Mateiu, Hans-Jørgen Albrechtsen and Barth F. Smets
Appl. Environ. Microbiol. **2014, 80(22):7010. DOI: 10.1128/AEM.01959-14.**
Published Ahead of Print 5 September 2014.

AEM
Journals.ASM.org

Internal Porosity of Mineral Coating Supports Microbial Activity in Rapid Sand Filters for Groundwater Treatment

Arda Gülay,[a] Karolina Tatari,[a] Sanin Musovic,[a] Ramona V. Mateiu,[b] Hans-Jørgen Albrechtsen,[a] Barth F. Smets[a]

Department of Environmental Engineering, Technical University of Denmark, Kongens Lyngby, Denmark[a]; Center for Electron Nanoscopy, Technical University of Denmark, Kongens Lyngby, Denmark[b]

A mineral coating develops on the filter grain surface when groundwater is treated via rapid sand filtration in drinking water production. The coating changes the physical and chemical properties of the filter material, but little is known about its effect on the activity, colonization, diversity, and abundance of microbiota. This study reveals that a mineral coating can positively affect the colonization and activity of microbial communities in rapid sand filters. To understand this effect, we investigated the abundance, spatial distribution, colonization, and diversity of all and of nitrifying prokaryotes in filter material with various degrees of mineral coating. We also examined the physical and chemical characteristics of the mineral coating. The amount of mineral coating correlated positively with the internal porosity, the packed bulk density, and the biologically available surface area of the filter material. The volumetric NH_4^+ removal rate also increased with the degree of mineral coating. Consistently, bacterial 16S rRNA and *amoA* abundances positively correlated with increased mineral coating levels. Microbial colonization could be visualized mainly within the outer periphery (60.6 ± 35.6 μm) of the mineral coating, which had a thickness of up to 600 ± 51 μm. Environmental scanning electron microscopic (E-SEM) observations suggested an extracellular polymeric substance-rich matrix and submicron-sized bacterial cells. Nitrifier diversity profiles were similar irrespective of the degree of mineral coating, as indicated by pyrosequencing analysis. Overall, our results demonstrate that mineral coating positively affects microbial colonization and activity in rapid sand filters, most likely due to increased volumetric cell abundances facilitated by the large surface area of internal mineral porosity accessible for microbial colonization.

Rapid sand filtration is a widespread technology to produce drinking water from groundwater. Granular materials such as quartz sand or anthracite are typically used filter media, which provide surfaces for colonization of sessile microbial communities (1). Several electron donors in anoxic groundwater, among which NH_4^+, Mn^{2+}, Fe^{2+}, CH_4, and low levels of assimilable organic carbon can serve as energy sources for microbial growth (2). Among these chemical species, Mn^{2+} and Fe^{2+} are the dominant and most commonly occurring constituents in groundwaters (3). During filtration, Mn^{2+} and Fe^{2+} are converted to Fe^{3+} and Mn^{4+} by biological or chemical oxidation, and together with a number of other cationic species (e.g., Ca and Mg) they form metal oxyhydroxides (MetOOH) of low solubility (4). These hydroxides form mobile (5) or attached colloids (6), which can aggregate or coalesce with the filter material, yielding a mineral coating. Accumulation of such precipitates on the filter material can increase the hydraulic resistance across the filter and shorten the time intervals needed between backwashing to regain the hydraulic loss.

Although backwashing is expected to completely remove these precipitates, accumulated mineral coatings have been observed in many rapid sand filters (RSFs) operating for more than 10 years (7). Increased accumulation of a mineral coating on the filter material affects the physical characteristics of the uncoated filter material (8, 9, 39, 44). Mature filter material from 12 drinking water treatment plants (DWTPs) showed porosities up to 8 times and specific surface areas up to 11 times higher than those of uncoated sand (7). Additionally, mineral coating has been found to positively impact the adsorption of metal ions (Fe^{2+}, Mn^{2+}, and As^{3+}) from the inlet groundwater (10, 38, 45) and the sorption of bacterial cells from synthetic groundwater (11, 12).

Although mineral coatings have been commonly observed in RSFs, there are no published studies examining their impact on microbial colonization, activity, or diversity. However, since microorganisms in RSFs are sessile, a relation between filter material surface and attached microorganisms is expected, and any alteration in the filter material characteristics caused by mineral coating is expected to affect microbial communities in different ways.

We examined filter material from RSFs at different DWTPs and identified a strong correlation between the amount of mineral coating and the amount of extractable DNA. Observations suggested that biomass increased in proportion to increases in coating mass within a filter as well as in different filters. On the basis of these preliminary observations, we hypothesized that mineral coatings support microbial growth in RSFs. To test this assertion, we obtained and segregated filter material from two different depths of a well-functioning RSF into different size fractions. We examined these size fractions using several molecular and biokinetic techniques, employing nitrification and nitrifying prokaryotes as the model function and guild. In addition, these fractions were subjected to several physicochemical measurements,

Received 12 June 2014 **Accepted** 29 August 2014
Published ahead of print 5 September 2014
Editor: S.-J. Liu
Address correspondence to Barth F. Smets, bfsm@env.dtu.dk.
A.G. and K.T. contributed equally to this article.
Supplemental material for this article may be found at http://dx.doi.org/10.1128/AEM.01959-14.

doi:10.1128/AEM.01959-14

while internal structure and microbial localization were revealed by grain-scale confocal and electron microscopic observations. Finally, we observed the microbial colonization capacity of the filter material fractions by examining the mineral coating in pilot-scale RSFs operated with high NH_4^+ and P loading. Ultimately, all observations indicated that mineral coatings are porous and provide internal surface area that is available for microbial colonization, resulting in enhanced microbial density and activity.

MATERIALS AND METHODS

Preliminary investigations. A series of preliminary investigations aimed to elucidate the relationship of mineral coating to biomass present on the filter material. Filter material was collected from the top layer (0- to 0.1-m depth) of the full-scale (FS) filters at DWTP 1 and DWTP 2 and of a pilot-scale (PS) filter at DWTP 2 (DWTP 2-PS) using a custom-made metal handler. DWTP 1 is located in Islevbro in the greater Copenhagen area, and DWTP 2 is in Marbjerg, Denmark (see description in the supplemental material). Furthermore, filter material was collected at different depths of the filters at Sjælsø-1 (DWTP 3), Sjælsø-2 (DWTP 4), and Langerød (DWTP 5), all located in Denmark (see description in the supplemental material). Core samples were collected at three random horizontal locations in each filter using Plexiglas tubes (internal diameter of 12 cm; length of 65 cm), and each core was sliced into the different depth sections. The samples were immediately transferred to the laboratory on ice, where DNA and mineral coating were extracted as described below.

Sampling and experimental design of the main investigations. The main investigations took place in DWTP 1, which treats anoxic groundwater abstracted from different nearby aquifers. In brief, the groundwater is first oxygenated to saturation by air injection in an aeration chamber (see Fig. S1 in the supplemental material). Fe^{2+} is allowed to be oxidized to Fe^{3+} and precipitated on the filter bed of the prefilters. The water is then led to the after-filters, designed to remove the remaining electron donors (NH_4^+, residual Fe^{2+}, and Mn^{2+}) mainly by biological processes, and thus our study focused on this step. After-filters have a 0.7-m-deep bed of quartz sand with a nominal average grain size of 0.8 to 1.2 mm, supported by a 0.3-m layer of coarser material. Treated water is supplied to the distribution system without chlorination. Influent and effluent water were sampled and analyzed for chemical composition (Table 1). Dissolved oxygen and pH were measured on site (WTW Oxi 340i with 325 CellOx and SenTix 41 WTW probes, respectively), while NH_4^+ and NO_2^- were measured colorimetrically (Spectroquant test kits 1.14752 and 1.14776; Merck). Metal concentrations were determined by inductively coupled plasma optical emission spectrometry (ICP-OES) (Vista-MPX CCD Simultaneous ICP-OES; Varian), using a customized stock solution (Inorganic Ventures) that included most metallic elements and phosphorus. Filter material for the main investigations was collected by core sampling as described above. From the obtained core two depth layers, top (0 to 0.1 m) and middle (0.2 to 0.3 m), were divided and transported to the lab on ice.

A fraction of the filter material from each depth layer (top and middle) of DWTP 1 was dried overnight at 60°C, and the particle size distribution was determined by sieving (vibratory sieve shaker AS 200 control; Retsch, Germany). In the top layer, 97% (mass-based percentage) of particles had a diameter of 1.0 to 2.5 mm, and 28% of middle-layer sand grains had a diameter of 1 to 2 mm, while 67% had a diameter of 0.5 to 1.0 mm. We segregated the remaining filter material from each depth into two fractions, one of larger and one of smaller particles, ultimately generating four filter material samples. The top layer was segregated into fractions with grain sizes of 2.0 to 2.4 mm (T 2.0–2.4) and 1.0 to 1.4 mm (T 1.0–1.4), while the middle layer was segregated into fractions with grain sizes of 1.0 to 1.4 (M 1.0–1.4) and 0.6 to 1.0 (M 0.6–1.0) mm. This segregation by depth and particle size created four filter material samples with different mineral coating properties that were used to investigate the relation of mineral coating to the microbiological processes.

TABLE 1 Chemical composition of the groundwater and influent and effluent of the after-filters at DWTP 1

Parameter (units)	Value in[a]:		
	Groundwater	RSF influent	RSF effluent
Dissolved oxygen (mg/liter)	1.10	9.25	8.60
pH	7.37	7.38	7.32
Total alkalinity (HCO_3^- [meq/liter])	NM	5.50	5.40
NH_4^+-N (mg/liter)	0.34	0.13	ND
NO_2^--N (μg/liter)	8.00	8.00	17.0
NO_3^--N (mg/liter)	NM	0.46	0.58
NVOC (mg/liter)[b]	NM	1.93	2.41
CH_4 (mg/liter)	0.03	NM	NM
H_2S (mg/liter)	0.02	NM	NM
SO_4^{2-} (mg/liter)	NM	32.2	33.1
PO_4^{3-}-P (μg/liter)	NM	13.0	3.00
Cl^- (mg/liter)	NM	62.5	62.8
Mn^{2+} (mg/liter)	0.06	0.04	ND
Fe total (mg/liter)	1.07	0.16	0.03
Fe^{2+} (mg/liter)[c]	NM	0.11	0.07
Fe^{3+} (mg/liter)	NM	0.05	ND
Al (mg/liter)	NM	0.19	0.30
Ba (mg/liter)	NM	0.06	0.13
Ca (mg/liter)	NM	140	144
Cd (mg/liter)	ND	0.17	0.40
Co (μg/liter)	NM	ND	0.08
Cr (μg/liter)	ND	1.64	1.33
Cu (μg/liter)	NM	ND	87.2
K (mg/liter)	NM	3.78	6.01
Mg (mg/liter)	NM	24.8	25.5

[a] NM, not measured, ND, not detected. Limits of detection: NH_4^+-N, 0.01 mg/liter; Mn, 0.001 mg/liter; Fe, 0.001 mg/liter; Co, 0.3 μg/liter; Cu, 1.4 μg/liter.
[b] NVOC, nonvolatile organic carbon.
[c] Differentiation between Fe^{2+} and Fe^{3+} was done by filtration of the water with a 20-μm disposable filter right after sample collection.

Determination of physical and chemical properties of the coated filter material. The drained wet mass of the four filter material samples was determined by passive drainage for 10 min. The packed volume of the samples was measured in a graduated cylinder that initially contained 25 ml of water. The drained wet packed bulk density was calculated from the packed bulk volume and the respective drained wet mass. The porosity of the filter material was a combination of the internal pore volume (intragrain volume) and the external pore volume (intergrain volume), and we estimated both volumes by measuring the water displacement in the graduated cylinder. Specifically, because the wet filter material was drained before packing, the internal pores were considered already filled with water, while the external pores were filled with water after the filter material was packed in the graduated cylinder. The external pore volume was estimated from the water displacement volume in the graduated cylinder by subtracting the water displacement volume from the packed bulk filter material volume.

The four filter material samples were dried at 60°C overnight and weighed again to calculate the dry to drained wet mass conversion factor. The dried filter material was then packed in a graduated cylinder as described previously to estimate the total pore volume (internal and external) from the water volume displacement in the graduated cylinder. The difference between total and external pore volume was an estimate of the internal filter material pore volume. The number of grains per volume of packed bulk filter material was manually counted in triplicate. Bulk packed density and internal pore volume were estimated in triplicate for each sample.

The external surface area per volume of packed bulk filter material was

calculated assuming spherical grains with an average diameter in each sample, i.e., 2.2 mm for the T 2.0–2.4 sample, 1.2 mm for the T 1.0–1.4 and M 1.0–1.4 samples, and 0.8 mm for the M 0.6–1.0 sample. The external surface area calculated for each grain was multiplied by the number of grains per volume of packed bulk filter material. The specific pore surface area of each filter material sample was estimated by Brunauer-Emmett-Teller (BET) sorption-desorption isotherms (Gemini III 2375 Surface Area Analyzer; Micromeritics). Before analysis, the samples were out-gassed with N_2 (FlowPrep 060 degasser; Micromeritics) for 24 h at room temperature. The method estimated the specific surface area of the internal pores sized between 2 and 32 nm.

In both the preliminary and the main investigations, the mineral coating was extracted from the filter material by acid digestion. Two grams of dry sand from each sample was digested with 2 ml of 65% HNO_3^- and 6 ml of 37% HCl for 3 h at 80°C. The samples were then cooled at room temperature, 2 ml of 30% H_2O_2 was added, and samples were heated to 80°C for 1 h to remove the organic carbon fraction from the sand surface (13). Samples were then dried overnight at 60°C before being weighed again, and the difference in mass before and after the mineral coating extraction was equal to the mineral coating mass present in each sample.

Nitrification activity of the filter material. Nitrification activity of the four filter material samples from DWTP 1 was quantified in a biokinetic assay described in detail elsewhere (14). Four lab-scale column filters were packed with the four filter material samples and were operated continuously for 2 days at a volumetric loading rate of 35 g of NH_4^+-N/m^3/day (per volume of packed filter material). Effluent water from the investigated full-scale rapid sand filter was used for the column influents, supplemented with 1 mg/liter NH_4^+-N as NH_4Cl (Merck Chemicals). The effluent NH_4^+ and NO_2^- concentrations were monitored at regular times (two to three times a day) by manual sampling and colorimetric analysis, giving a total of five data points for each column under this loading condition, as described above. At day 2 after start-up, the influent loading was up-shifted to 350 g of NH_4^+-N/m^3/day, and the effluents were monitored and sampled every 30 min for 4 h, giving a total of four measurements from each column. The duration of experiments was intentionally short to avoid substantial growth of nitrifying biomass in the filters. During column operation at each of the two loading rates, the effluent concentration stabilized at a different NH_4^+ levels. The NH_4^+ volumetric (per volume of packed filter material) removal rate was calculated from the difference between influent and effluent (after it stabilized) NH_4^+-N loading, divided by the packed bulk filter material volume in the filter and averaged over the available data points for each loading condition.

Microbial colonization capacity experiments. Two pilot-scale filters were inoculated with filter material from the full-scale filter at DWTP 1 as described elsewhere (15) and were operated at high NH_4^+ and P concentrations (see the supplemental material). After 45 days of operation at high-NH_4^+ and high-P influent loading (see detailed description in the supplemental material), filter material was collected from the 0- to 0.1-m (top)- and 0.2- to 0.3-m (middle)-depth layers of both pilot-scale filters and was segregated into size fractions of 2.0 to 2.4 and 1.0 to 1.4 mm for the top layer and of 1.0 to 1.4 and 0.6 to 1.0 mm for the middle layer. With these investigations we examined whether this increase in NH_4^+ and P loading resulted in increased microbial density and whether such a microbial density increase could be visualized using microscopic and molecular techniques. Real-time PCR and confocal laser scanning microscopy (CLSM) imaging were used on these fractions, as described below.

Cryosectioning, live and dead staining, and CLSM imaging. The filter material samples collected from the full- and pilot-scale filters of DWTP 1 were fixed by 4% paraformaldehyde, embedded in 22-oxacalcitriol (OCT) compound (TissueTek; Sakura, The Netherlands), and frozen at −20°C. The mineral coatings of three representative sand grains from each size fraction of the top layer of both filters were cut in 20-μm thin sections by a microtome and mounted on gelatin-coated glass slides (16). The samples originating from the middle layer could not be cut by the microtome because of the small amounts of mineral coating. The retrieved 10 sections from each representative grain were dehydrated and sequentially stained with a Live/Dead BacLight viability kit (L7012; Molecular Probes/Invitrogen, USA) according to the manufacturer's specifications. Live/Dead staining distinguishes microorganisms that have damaged (dead) and nondamaged (live) cell membranes. Stained sections were analyzed with a confocal laser scanning microscope ([CLSM] TCS SP5; Leica, Germany) equipped with an Ar laser (488 nm), using 20× and 64× objectives. SYTO (SYTO9; Invitrogen, Carlsbad, CA, USA)-stained and propidium iodide-stained images were analyzed with a Leica AS AF Lite (Leica, Germany) instrument and ImagePro (MediaCybernetics, USA) software to observe the spatial distribution of cells within the mineral coating.

High-vacuum SEM (HV-SEM) and E-SEM. Cryosections from the T 2.0–2.4 sample of the full-scale filter were visualized with a scanning electron microscope (SEM) (Quanta 200 F FEG; FEI) used both for environmental SEM (E-SEM) and regular SEM observations. For the E-SEM, the sections were placed on an aluminum tap with double-sided carbon tape and imaged at a partial water pressure of 1.0×10^6 mPa with a secondary gaseous electron detector. Energy-dispersive X-ray spectroscopy (EDS) was conducted on the mineral coating of the T 2.0–2.4 filter material samples with an 80-mm X-Max silicon drift detector (Oxford Instruments) coupled to the microscope. For the SEM, the coating sections obtained by cryosectioning were similarly mounted on an aluminum tap with a double-sided carbon tape and imaged at high vacuum with an Everhart-Thornley detector.

SEM images were analyzed and calibrated with ImagePro (MediaCybernetics, USA) software to reveal the pore area distribution of the investigated coating sections at different scales.

DNA extraction. Drained wet filter material (0.5 g) from DWTPs 1 to 5 (preliminary and main investigations) were subjected to genomic DNA extraction using a FastDNA Spin kit (MP Biomedicals, Solon, OH, USA) according to the manufacturer's instructions at room temperature. The concentration and purity of extracted DNA were checked by a NanoDrop 2000 spectrophotometer (NanoDrop Technologies, Wilmington, DE, USA).

PCR, pyrosequencing, and bioinformatic analyses in the main investigations. Ten nanograms of extracted DNA from the four samples from DWTP 1 was PCR amplified using Phusion (*Pfu*) DNA polymerase (Finnzymes, Finland) and 16S rRNA gene-targeted modified universal primers PRK341F (5′-CCTAYGGGRBGCASCAG-3′) and PRK806R (5′-GGACTACNNGGGTATCTAAT-3′) (17). PCR was performed as described elsewhere (18). The process of adapter- and sample-specific tag addition and further amplicon quantification were done as described elsewhere (19). Pyrosequencing was applied in a two-region 454 run on a GS PicoTiterPlate (70- by 75-mm format) using a titanium kit and GS FLX pyrosequencing system at the National High-Throughput DNA Sequencing Center (University of Copenhagen, Copenhagen, DK) according to the manufacturer's instructions (Roche) and as previously described (20).

All raw 16S rRNA gene amplicons were denoised, processed, and classified using the QIIME (http://qiime.org/index.html) software package (21). Chimera checking was performed with the software UChime (22). High-quality sequences were clustered at 97% evolutionary similarity and aligned against the Greengenes reference set (23) using the PyNAST algorithm (24). Taxonomy assignment of each representative sequence was implemented using the BLAST algorithm (25) against the Silva 108 curated database (26). All diversity estimations were performed using algorithms in QIIME software.

Extracted nitrifier sequences based on taxa at the genus level (see Table S1 in the supplemental material) were transferred to web-based SINA, version 1.2.11 (27), for alignment and selection of the top 10 closest relatives for each sequence. Aligned sequences were then imported into the ARB software environment (28) for phylogenetic tree construction. Statistical calculations and phylogenetic comparisons were carried out using R software (R Development Core Team, 2012). A detailed description of the bioinformatics analysis is provided in the supplemental material.

TABLE 2 Physical properties of the four investigated filter material samples collected and segregated by size from the full-scale after-filter at DWTP 1

Parameter	Value for indicated fraction[a]			
	T 2.0–2.4	T 1.0–1.4	M 1.0–1.4	M 0.6–1.0
Sampling depth in filter bed (m below surface)	0–0.1		0.2–0.3	
Grain size of filter material (diam range [mm])[b]	2.0–2.4	1.0–1.4	1.0–1.4	0.6–1.0
Mass coating per vol of packed bulk filter material (kg/m^3)[c]	456	389	57	100
Density of drained wet packed bulk filter material (10^3 kg/m^3)[d]	1.11 (±0.05)	1.28 (±0.03)	1.56 (±0.12)	1.67 (±0.10)
Internal pore vol per vol of packed bulk filter material (m^3/m^3)[e]	0.63 (±0.03)	0.60 (±0.03)	0.28 (±0.03)	0.28 (±0.02)
No. of filter material grains per vol of packed bulk filter material (10^7 grains/m^3)	26.0 (±12)	44.0 (±16)	69.0 (±29)	136 (±78)
External surface area per vol of packed bulk filter material (10^3 m^2/m^3)[f]	1.6	3	3.1	3.1
BET-specific surface area per vol of packed bulk filter material (10^6 m^2/m^3)	41	35	5.4	8.6

[a] Standard deviation is reported for triplicate measurements
[b] Filter material sizes were quantified by sieving.
[c] Extracted by acid digestion of the coated filter material.
[d] Measured by the mass and volume of packed bulk filter material in a graduated cylinder.
[e] Estimated by water displacement of dry and drained wet sand in a graduated cylinder.
[f] External surface area was calculated from external surface area of an equivalent spherical sand grain and multiplied by the number of sand grains per volume of packed bulk filter material.

Real-time qPCR. Quantification of total bacteria (*Eubacteria*), ammonium-oxidizing bacteria (AOB), and ammonium-oxidizing archaea (AOA) was done by quantitative-PCR (qPCR) on the DNA extracted from the collected filter material samples.

A specific region on the 16S rRNA gene was amplified using the 1055F and 1392R primer sets for total *Eubacteria* (29). To quantify AOB and AOA, the specific regions of a functional, ammonia monooxygenase subunit A-encoding *amoA* gene were targeted by the amoA1F and amoA2R primer set for AOB (30) or the amoAF and amoAR primer set for AOA (31).

qPCR analyses were conducted in a Chromo4 thermocycler operated by Opticon Monitor, version 3, software (Bio-Rad). Each qPCR mixture contained 12.5 μl of 2× iQ SYBR green Supermix (Bio-Rad Laboratories), 500 nM primer, DNA template (10 ng), and DNA/RNA-free water (Mo Bio Laboratories) to 25 μl. The thermal cycling conditions consisted of an initial 5-min denaturation at 95°C, followed by 40 cycles of denaturation at 94°C for 30 s and primer annealing for 30 s, 30 s, and 60 s at 55°C, 56°C, and 60°C for total eubacteria, AOB, and AOA, respectively, with a 1-min extension at 72°C. The specific amplification was tested by a melting curve analysis (gradient, 0.2°C/s; range, 70 to 95°C) (32). The gene copy number was interpolated from a standard curve.

Statistical analysis. Pearson's product-moment correlation coefficient analysis was used to identify linear correlations between the estimated physical properties (packed bulk density, mass of coating extracted, and BET-specific surface area), the observed NH_4^+ removal rates, and the abundance of AOB, AOA, and total bacteria in the four filter material samples. All calculations were implemented using Sigma Plot (version 11).

Nucleotide sequence accession numbers. Sequences generated in this study were deposited in the European Nucleotide Archive (ENA) under accession numbers LN515613 to LN551923.

RESULTS

Preliminary mineral coating observations at different DWTPs. The first round of preliminary investigations aimed to identify the presence of mineral coating and microbes on the filter material of DWTP 1 and DWTP 2. As illustrated in Fig. S2 in the supplemental material, mineral coating was present in both full-scale filters but was detected at a very low degree on the filter material from the pilot-scale filter in DWTP 2. In these three filters we noted a positive linear correlation between the extracted DNA mass and the amount of coating on the filter material (see Fig. S2). Similarly, in the second round of preliminary investigations, the amount of DNA from different depths of the filters at DWTPs 1 and 5 increased with the amount of mineral coating present (see Fig. S3). A very low degree of mineral coating was detected at DWTPs 3 and 4. Overall, these observations suggested that a higher degree of coating results in higher microbial density on the filter material.

Physical and chemical characteristics of coated filter material. The four filter material samples collected for the main investigations (T 2.0–2.4, T 1.0–1.4, M 1.0–1.4, and M 0.6–1.0) were analyzed for their physical and chemical properties. In general the mass of mineral coating decreased with depth and with grain size, at least for the top-layer samples (T 2.0–2.4 and T 1.0–1.4) (Table 2). The bulk packed density of the filter material decreased with increasing mineral coating mass, corresponding to the increase in internal pore volume (per unit of filter material packed bulk volume). This was confirmed by internal pore volume estimates (Table 2), which, in combination with the packed bulk density measurements, indicated that the mineral coating determined the depth stratification of the filter material.

Consistently, the specific surface area estimated from the BET isotherms revealed that the filter material samples with more coating mass per unit packed bulk volume of filter material (57 to 456 kg/m^3) had the highest surface areas (5.4 to 41 m^2/m^3). Pairwise comparisons using the Pearson product-moment correlation showed a strong positive correlation ($r^2 = 1$, $P = 0.0001$) of mineral coating mass and BET-specific surface, whereas packed bulk density and BET-specific surface area showed a strong negative correlation ($r^2 = -0.98$, $P = 0.02$). Overall, these observations suggest that the mineral coating formed a porous mineral matrix around the original filter material. A clear image of the mineral coating on the filter material is shown in Fig. 1.

Moreover, the total BET surface area increased with internal pore volume and decreased with external surface area, indicating that the mineral coating creates internal surface area while decreasing the specific external surface area of the filter material (see Fig. S4 in the supplemental material).

Elemental analysis of the extracted mineral coating showed a predominance of Mn (26.4% ± 4.1%), Fe (14.4% ± 2.7%), and Ca (4.1% ± 0.8%), with small differences in relative mass percentages between the four filter material samples, and this distribution of chemical species did not differ appreciably between the filter materials; hence, no significant effect of coating composition on microbial communities was expected in the fractions of different

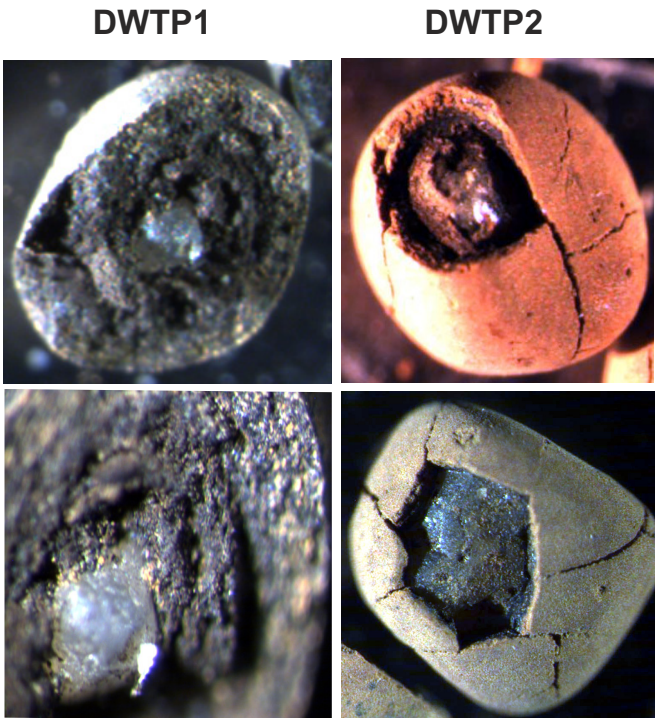

FIG 1 Stereomicroscope images show the original filter materials embedded inside the mineral coating.

grain sizes (Table S2). The observed elemental composition of the mineral coating is also consistent with the composition from other groundwater-treating DWTPs (7), with Fe and Mn as predominant elements in the mineral coating. Unidentified portions of the elemental composition (51.5% ± 8.4%) were most likely bicarbonate and hydroxide anions, in concordance with SEM-EDS analysis indicating C and O as major elements together with Mn and Fe (see Fig. S5 in the supplemental material).

Mineral coating architecture. SEM examination of the mineral coating from the T 2.0–2.4 filter material sample showed a diversity of micro- and macropore structures (Fig. 2) as well as dense accumulations of encrusted organic structures (Fig. 2d; see also Fig. S6 in the supplemental material) that were distinct from abiogenic minerals. SEM images also revealed the homogenous distribution of pores in the mineral coating (Fig. 2a). No channels were observed connecting the external surface to the deeper layers. The majority of pores from the pore throat area counts of the SEM images (at a scale of 200 and 400 μm) (Fig. 2a) were between 10 μm^2 and 200 μm^2 and accounted for 40.8% ± 34% of the total pore counts in the mineral coating of T 2.0–2.4 filter material, whereas pores of 5 to 10 μm^2 accounted for 31.3% ± 14% of the total pore counts (see Fig. S7a in the supplemental material). In addition, at higher magnification (at the scale of 20 μm) (Fig. 1b), 22.3% ± 2.68% of the total pore counts lay between the pore area of 0.1 to 1 μm^2 (see Fig. S7c), showing the presence of pores

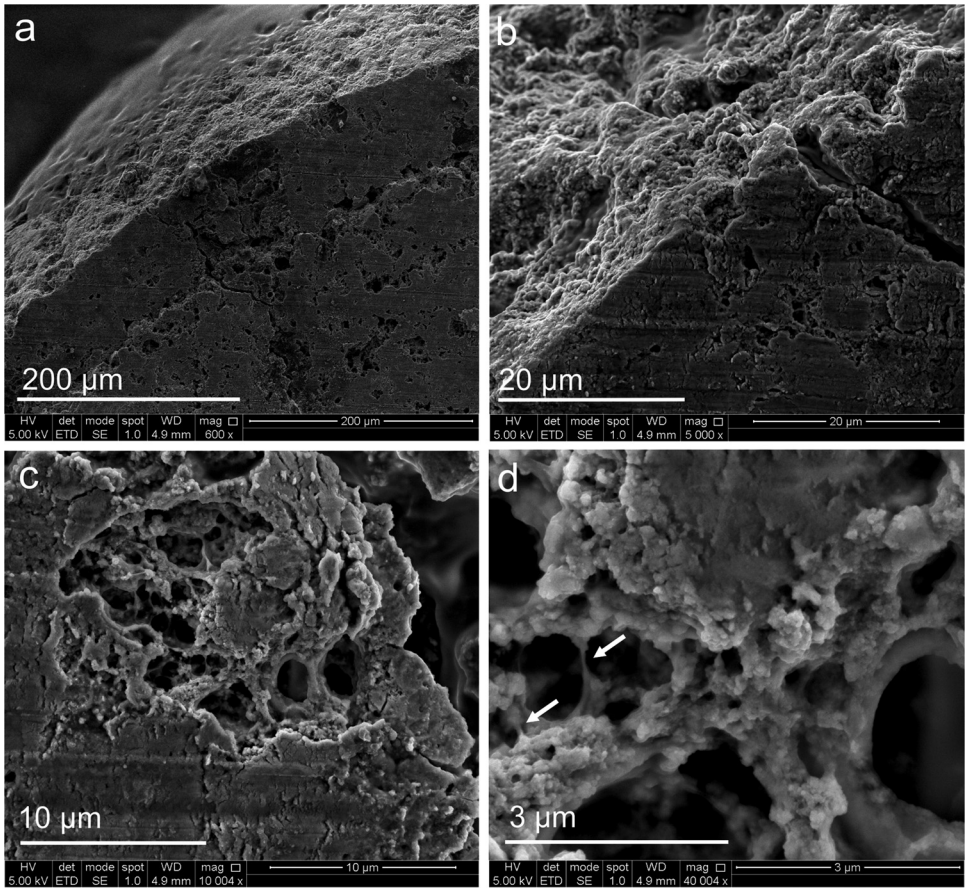

FIG 2 SEM images of cryosections across the mineral coating of a T 2.0–2.4 filter material sample. (a and b) External and internal view of the mineral coating. (c) Internal pore. (d) Encrusted organics and individual pore structures. Arrows indicate encrusted organic-like structures.

smaller than typical average single prokaryotic cell diameters (33). Altogether, a large portion of the detected pores in T 2.0–2.4 samples were deemed appropriate for microbial colonization.

Nitrification activity of coated filter materials. Nitrification activity of the four differently coated filter material samples (T 2.0–2.4, T 1.0–1.4, M 1.0–1.4, and M 0.6–1.0) revealed a significant increase in the volumetric NH_4^+ removal rate under both high- and low-loading conditions with increasing mineral coating mass (Fig. 3A) ($r^2 = 0.99$ and $P = 0.001$ at high loading, $r^2 = 0.99$ and $P = 0.003$ at low loading).

There was no significant correlation ($r^2 = 0.22$, $P = 0.77$) between the nitrification activity and the calculated external surface area per unit of grain volume. Therefore, a normalized bioavailable surface area (NBSA) estimate was used under the assumption that the area-specific NH_4^+ removal rates were equal for all four filter material samples. The area-specific NH_4^+ removal rate was calculated by dividing the observed NH_4^+ removal rate at the highest loading rate (350 g of NH_4^+-N/m^3/day) by the external surface area per packed bulk volume unit (Table 2) for the least-coated filter material (57 kg/m^3). This calculation implied that the NBSA of the least-coated filter material sample (M 1.0–1.4) is equal to the external surface area because of the negligible internal pore area of this fraction. The NBSA was calculated for the three other filter material samples by dividing the measured nitrification activity under the high-loading condition by the area-specific NH_4^+ removal rate. The estimated NBSA increased with increasing mineral coating mass on the filter material ($r^2 = 0.96$, $P = 0.04$) (Fig. 3B), and the experimentally obtained BET-specific surface area (Fig. 3B) was significantly and positively correlated with the estimated NBSA ($r^2 = 0.95$, $P = 0.04$).

Spatial distribution of microorganisms within the mineral coating. The cryosectioned filter material samples from the top filter layer (T 2.0–2.4 and T 1.0–1.4) were visualized by CLSM. Microorganisms detected with DNA-binding stain (green fluorescence) (Fig. 4b to e for T 2.0–2.4; see also Fig. S8b in the supplemental material for T 1.0–1.4) were visible in the outer periphery of the mineral coating and colocalized with dead-cell signals (red fluorescence) (Fig. 4c to f for T 2.0–2.4; see Fig. S8c for T 1.0–1.4).

Microbial clusters were homogeneously distributed inside the mineral coating and up to 120 μm below the outer surface, with an average biofilm thickness of 15 μm. The average coating depth where most cells were found was 60.6 ± 35.6 μm and 12.3 ± 5.5 μm for the T 2.0–2.4 and T 1.0–1.4 filter material samples, respectively. Sporadic cell signals were detected in the deeper parts of the mineral coating, suggesting that these layers are possibly inactive zones for microbial activity. Microbial cells were primarily organized in spatially separate microbial clusters instead of thick and continuous biofilms, suggesting internal isolation of microbial communities in a single filter material due to the dissociated internal pores of the mineral coating.

Visualization of microbial cells and EPS within the mineral coating. E-SEM images of the T 2.0–2.4 filter material sample showed a white nebulous network with branching filaments attached to the surfaces of the internal pores (Fig. 5). Intriguingly, coccoid microbial cell-like structures with an average diameter of ca. 0.2 μm were observed in all analyzed micrographs. Coccoids as well as white nebulous network structures were not observed in SEM images due to the high-vacuum condition in SEM examination, which destroys organic structures. Cells were embedded inside an organic network that strongly resembled extracellular polymeric substances (EPS). Observation of such organic matrices is, however, surprising in this oligotrophic environment (34), given the low assimilable organic carbon content in the influent water. As a conclusion, the E-SEM images suggest microbial colonization within the mineral coating of the internal pores.

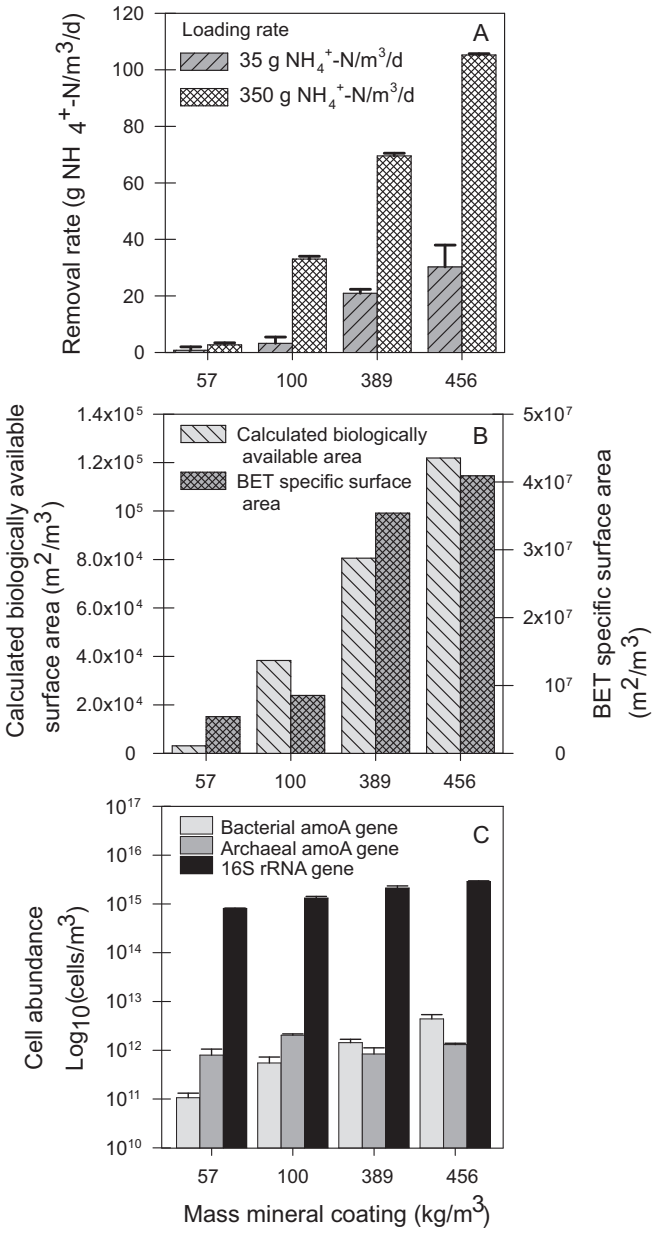

FIG 3 (A) Volumetric NH_4^+ removal rate at high- and low-ammonium loadings for filter material samples with different coating masses per filter material packed volume. (B) Area equivalents for filter material with different coating masses per filter material packed volume. (C) Archaeal and bacterial *amoA* and bacterial 16S rRNA gene copy equivalents for filter material with different coating masses per filter material packed volume.

Microbial abundance in coated filter materials. Microbial abundance in the four filter material samples was measured by qPCR targeting both the 16S rRNA and the *amoA* genes. Bacterial 16S rRNA abundances (expressed as the number of gene copies/m^3 of packed bulk filter material) increased and significantly

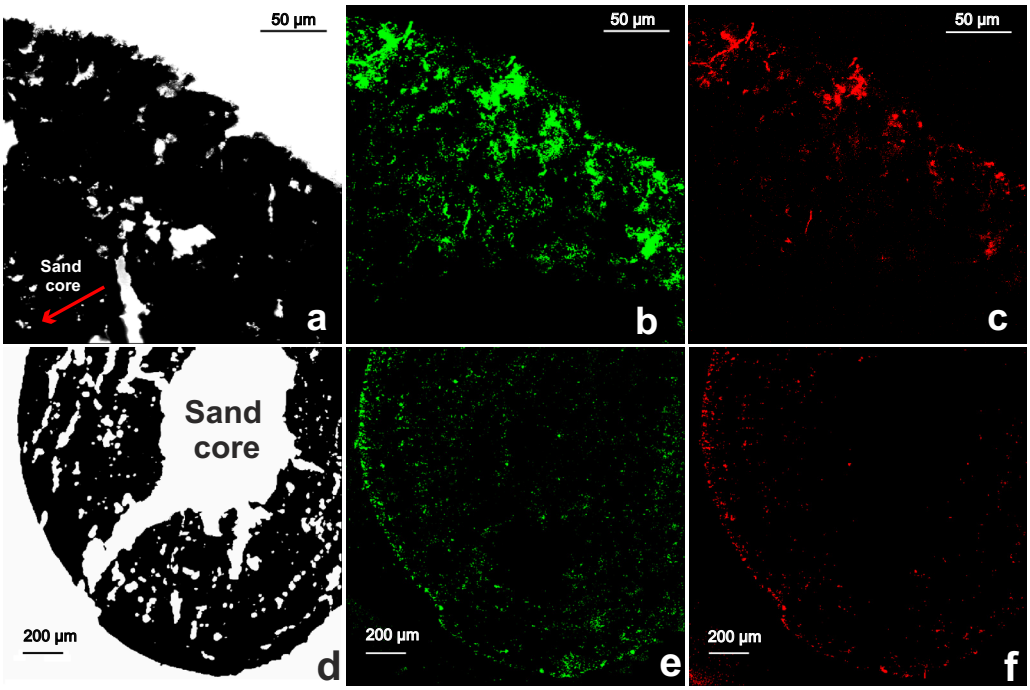

FIG 4 Confocal laser scanning micrographs of a cryosectioned mineral coating layer from the T 2.0–2.4 filter material sample showing the spatial distribution of microorganisms. Visualization of the outer periphery (a, b, and c) and of the complete cross section of the mineral coating (d, e, and f) using differential interference contrast observation without staining and (a and d) and using fluorescence observation with SYTO9 (green; b and e) and propidium iodide staining (red; c and f).

correlated with an increasing degree of coating ($r^2 = 0.96$, $P = 0.03$). An increase in bacterial 16S rRNA abundance was also correlated with an increase in the nitrification rates ($r^2 = 0.97$ and $P = 0.02$ for low-loading and $r^2 = 0.96$ and $P = 0.04$ for high-loading conditions) measured by the activity assay. Likewise, bacterial 16S rRNA gene copy numbers exhibited a significant positive correlation with the BET-specific surface area ($r^2 = 0.96$, $P = 0.04$). Together, these results suggest a strong density-function-colonization relation between mineral coating presence and bacterial biomass. The abundance of *amoA* copies (Fig. 3C) increased consistently with increases in the coating mass, surface area, and nitrification activity (see Fig. S4 in the supplemental material). Archaeal *amoA* gene abundances were higher in the middle-layer samples (M 1.0 to 1.4 and M 0.6 to 1.0) than in the top-layer samples (T 2.0 to 2.4 and T 1.0 to 1.4). However, unlike the bacterial *amoA* and total 16S rRNA gene abundances, no linear correlation was detected between coating mass, nitrification rates, and archaeal *amoA* gene abundances (see Fig. S4).

Microbial diversity and composition in coated filter materials. The four filter material samples were 454 pyrosequenced to assess nitrifier diversity in each filter material fraction and to identify similarities in nitrifier composition between filter material fractions. A total of 39,224 sequences passed through quality checks (with denoising and chimera removal) and were further distributed across 1,949 operational taxonomic units (OTUs) at a 97% ($OTU_{0.03}$s) nucleotide sequence identity threshold. High-quality sequences were normalized by rarefying to 7,000 sequences per sample for further diversity and taxonomic comparisons.

The analysis of the unweighted and weighted UniFrac distances showed no significant differences in community compositions of known AOB and AOA between the four filter grain fractions (see Table S3 in the supplemental material), indicating that the NH_4^+ oxidation metabolisms were similar (Fig. 6). Likewise, the phylogenetically based comparisons showed insignificant differences between total microbial community compositions (see Table S3). Together, these results suggest that the difference between the volumetric nitrification rates observed for the four filter material samples in the activity assays is not related to different AOB phylogenies.

Evenness and taxonomic richness in the filter material samples revealed that changes in coating mass or internal surface area did not strongly influence these diversity components as no significant linear correlation was detected (see Table S4 in the supplemental material). Faith's phylogenetic distance estimations also showed an insignificant correlation with coating mass (see Table S4). Sequences closely related to the *Archaea* domain were solely detected in filter material from the middle layer, confirming the quantification results from the *amoA* gene-based qPCR.

Links between microbes and mineral coating were further investigated by correlating specific OTUs at a 97% similarity threshold and taxa at the phylum taxonomic level with coating mass using significant ($P < 0.01$) and strong ($r^2 > 0.97$) Pearson relations and network analysis (for the phylum level, see Fig. S9, and for the $OTU_{0.03}$ level, see Fig. S10 in the supplemental material). Among 1,949 $OTU_{0.03}$s, only 20 were significantly correlated with the coating mass. Positively correlated taxa (13 $OTU_{0.03}$s) were mainly related to the candidate division OD1, *Firmicutes*, *Bacteriodetes*, and *Proteobacteria*, and negatively correlated taxa

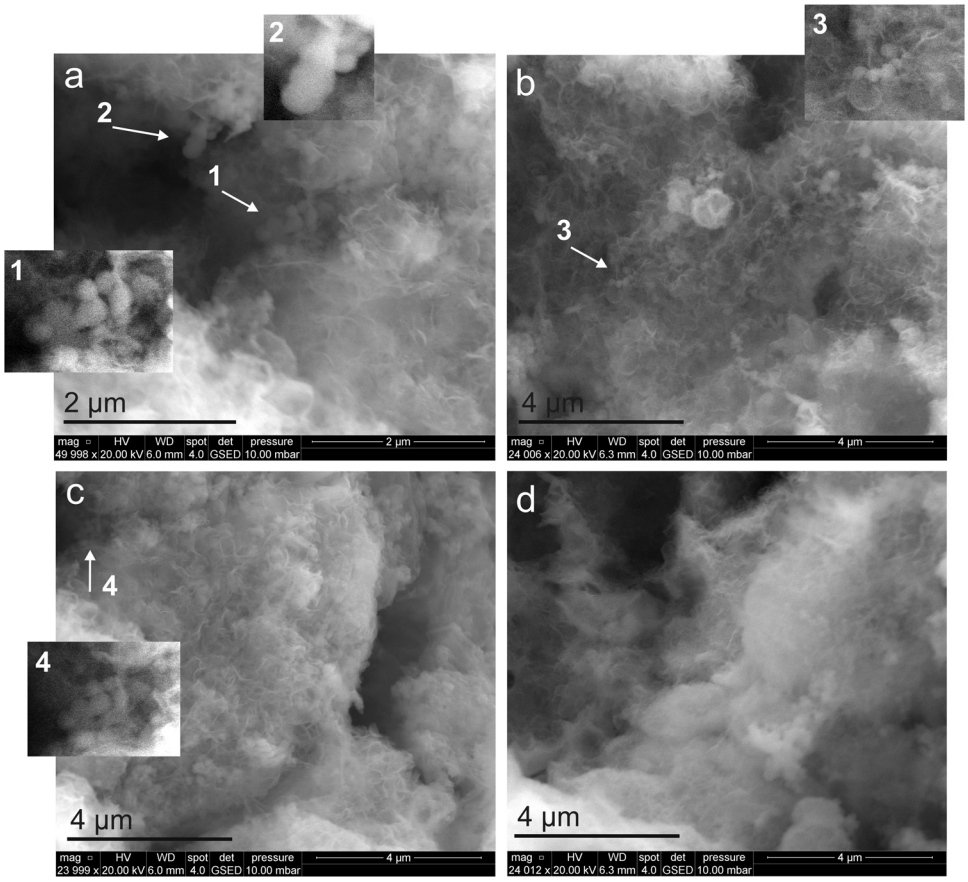

FIG 5 E-SEM images of the mineral coating from a T 2.0–2.4 filter material sample, showing internal pores, organic structures, and coccoid cell-like structures. Zoomed regions showing coccoid clusters are indicated by arrows and numbers.

($OTU_{0.03}$s) were related to the *Proteobacteria*, candidate division TM7, *Chloroflexi*, and candidate division SR1 at the phylum level.

Microbial colonization capacity of mineral coating. We used two parallel pilot-scale filters at DWTP 1 (15) to investigate the colonization potential of the filter material by exposing the filters to increased substrate (NH_4^+) and nutrient (P) conditions (see the description in the supplemental material). In both PS filters, the removal rate increased with increasing NH_4^+ and P loading rates (46). Filter materials at the same depth and size fractions consistent with those examined in this study were subjected to bacterial 16S rRNA quantification and microscopic inspection. Microbial abundance measured by 16S rRNA gene-targeted qPCR consistently increased (up to 1 order of magnitude), regardless of the size and amount of the mineral coating (Fig. 7a). In addition, it was visually confirmed that the cell density increased in the internal pores of the mineral coating and not on the external surface area of the filter material (Fig. 7b and c). The average biofilm depths now increased to 145 ± 77 μm for T 2.0–2.4 and to 66 ± 19 μm for T 1.4–1.6 filter material samples.

DISCUSSION

Changes in abiotic phases due to the presence of mineral coating. DWTP 1 is an RSF-based plant treating anoxic groundwater with a significant Fe^{2+} concentration. Extraction of the mineral coating from the filter material and examination of differently coated materials revealed that packed bulk density decreased with increases in the degree of coating. Such a negative relationship between mineral coating and filter material density in RSFs has been reported before (7, 35) and could be the primary cause of vertical stratification even though the filter is periodically backwashed. The mechanism of mineral coating formation has been previously linked to adsorption of Fe^{2+} coupled with oxidation (36) and to the attachment of small iron particles (<1.0 μm) coupled with consolidation (37). These scenarios postulate that the newly formed coating proliferates on the surface of a preformed coating. This is in accordance with our SEM images, in which encrusted biological structures were observed in the inner coating layer (>120 μm) although no living cells were detected there by confocal imaging. A possible explanation for the zones without cells in the inner layers could be the limitation of nutrient diffusion into the inner layers due to the high microbial activity in the outer periphery of the coatings. This is consistent with our results from microbial colonization capacity experiments; microbial growth in the inner pores (average depths of 145 ± 77 μm and 66 ± 19 μm for T 2.0–2.4 and T 1.0–1.4 filter material samples, respectively) was detected when filter materials were exposed to higher NH_4^+ and/or P loading than under full-scale operating conditions.

The surface area measurements and electron micrographs indicate that mineral coating increases the internal porosity available for microbial colonization. This increase in internal surface

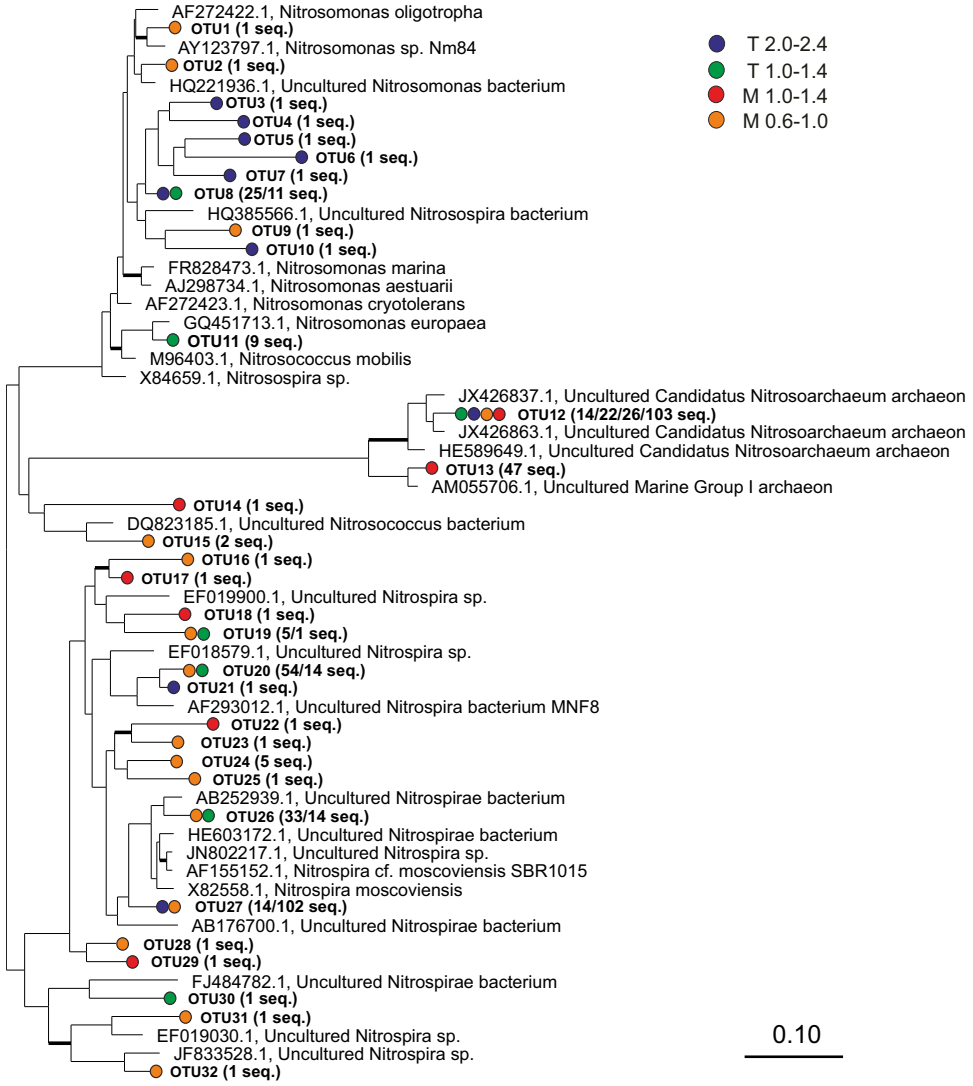

FIG 6 Phylogenetic tree of $OTU_{0.03}$s related to taxa of $NH4^+$-oxidizing and NO_2^--oxidizing prokaryotes in the investigated filter material samples. The tree was constructed using the neighbor-joining algorithm in ARB with 1,000 bootstrap replicates. The percentage of replicate trees (>60%) are shown by thick branches. The scale bar represents 0.10 substitutions per nucleotide position. The numbers in parentheses refer to the observed sequences in each $OTU_{0.03}$. Filter grain fractions are as indicated on the figure. seq, sequence(s).

area has been suggested to affect cell (11) and metal adsorption (38) from groundwaters, mainly because mineral complexes can contain active adsorption sites (39). However, the latter effects were not examined in this study.

Changes in the biotic phase due to the presence of a mineral coating on the filter material. Concomitant qPCR, biokinetic, and microscopic analyses of coated filter material samples showed that microbial abundance and activity increased with an increase in the presence of the mineral coating. Second, both total (16S rRNA gene) and functional (*amoA*) bacterial abundances are strongly and positively correlated with the measured volumetric NH_4^+ removal rates at both low and high loading rates for the investigated size fractions (see Fig. S4 in the supplemental material). Together with spatial distribution and microbial abundance patterns, this indicates that aggregation of the mineral coating positively affects microbial activity by supporting the total and functional microbial densities. Furthermore, phylogenetic analysis suggested that the NH_4^+-oxidizing types in differently coated filter material samples were similar, which strengthens our interpretation that the mineral coating supports higher nitrifier abundance and activity. Considering the microbial colonization capacity and spatial microbial distribution experiments, it is more likely that the internal pore surfaces of the mineral coating create solid-liquid interfaces wherein microbes utilize substrate and grow and are protected from wash-out, as might occur during filter backwashing. Hence, the greater the pore surface area (with the average biofilm depths of 60.6 ± 35 μm for T 2.0–2.4 and 12.3 ± 5 μm for T 1.0–1.4 grain fractions from the outer boundary; no biofilms were detected below this range) (Fig. 4b and c), the more biomass that can be supported. This mechanism could also lead to an increase in abundance of functional groups (for example, AOB abundances) (Fig. 3) with increases in the degree of coating due to better accessibility of substrates and nutrients. The abundance of NH_4^+-oxidizing archaea (AOA), on the other hand, did not

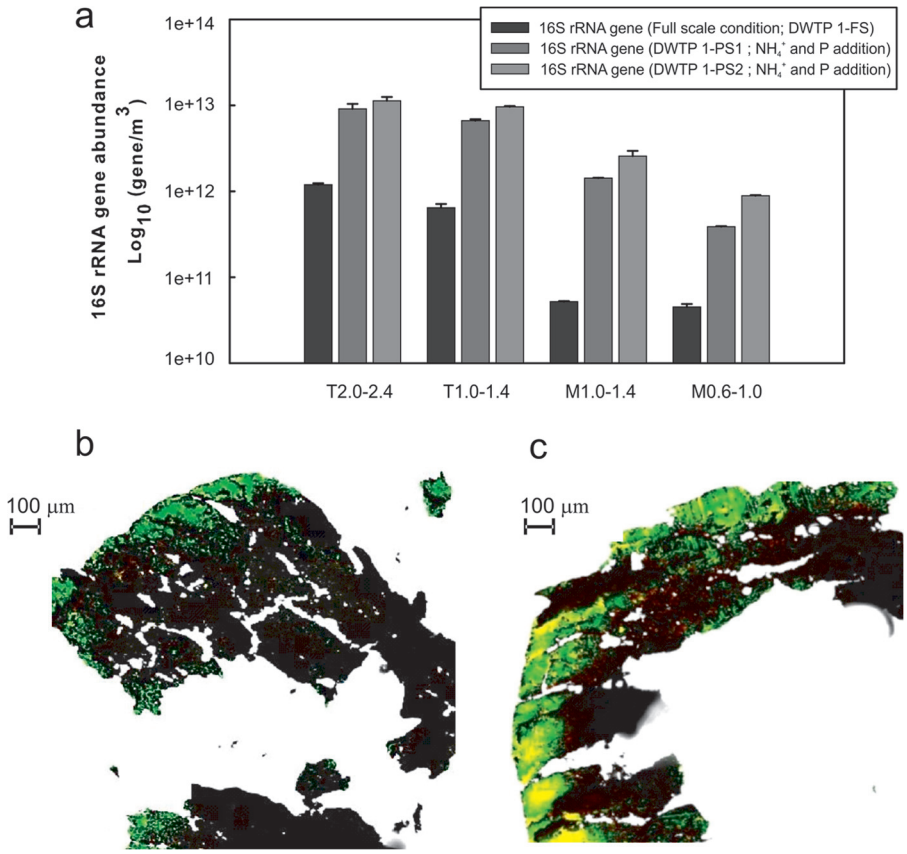

FIG 7 (a) Bacterial 16S rRNA gene copy equivalents for grains with different sizes from one full-scale (DWTP 1-FS) and two pilot-scale (DWTP 1-PS1 and DWTP 1-PS2) filters. CLSM images of the cryosectioned mineral coating layer from a T 2.0–2.4 filter material sample of the full-scale filter (b) and the pilot-scale filter (c) show the spatial distribution of microorganisms (green, SYTO9 stain; yellow, propidium iodide with SYTO9 stain).

change monotonically with coating mass; instead, it was higher for the less coated filter material from the deeper filter layer (see Table S5 and Fig. S11 in the supplemental material). This is potentially attributed to different niche preferences than those of AOBs, such as low tolerance for high NH_4^+ concentrations and higher NH_4^+ affinities (40, 41). Microbial colonization experiments, facilitated by increasing the NH_4^+ and P load, indicated the availability of inner pores for microbial colonization.

EPS compounds have previously been identified on the surface of filter materials in different RSFs (42, 43). Our E-SEM images confirm the presence of EPS and embedded biofilms, but, in contrast to previous findings (42, 43), they were detected in the internal pores of the mineral coating rather than on the external surface.

Concluding remarks. In contrast to the presumed negative effect of coatings on microbes, our results demonstrate the strong positive effect of a mineral coating on microorganisms in RSFs. The large internal porosity of the mineral coating supports microbial colonization, resulting in higher NH_4^+ removal rates and microbial densities. These positive correlations suggest that the mineral coating plays a protective and supportive role in microbial colonization, density, and activity in RSFs treating groundwater.

ACKNOWLEDGMENTS

We thank George Kwarteng Amoako for assistance in sample collection and all personnel at the Islevbro Water Treatment Plant for access to their facilities. We also thank Sinh Hy Nguyen and Annie Ravn Petersen for technical assistance and Carson O. Lee for samples from his pilot plant.

This research was financed by The Danish Council for Strategic Research (Project DW Biofilter).

REFERENCES

1. **Sharma SK, Greetham MR, Schippers JC.** 1999. Adsorption of iron(II) onto filter media. Aqua **48:**84–91.
2. **Bai Y, Liu R, Liang J, Qu J.** 2013. Integrated metagenomic and physiochemical analyses to evaluate the potential role of microbes in the sand filter of a drinking water treatment system. PLoS One **8:**e61011. http://dx.doi.org/10.1371/journal.pone.0061011.
3. **Søgaard EG, Madsen HT.** 2013. Groundwater chemistry and treatment: application to Danish waterworks, p 223–246. *In* Elshorbagy W, Chowdhury RK (ed), Water treatment. InTech, Rijeka, Croatia.
4. **Teunissen K, Abrahamse A, Leijssen H, Rietveld L, van Dijk H.** 2008. Removal of both dissolved and particulate iron from groundwater. Drink. Water Eng. Sci. Discuss. **1:**87–115. http://dx.doi.org/10.5194/dwesd-1-87-2008.
5. **Wolthoorn A, Temminghoff EJM, van Riemsdijk WH.** 2004. Effect of synthetic iron colloids on the microbiological NH_4^+ removal process during groundwater purification. Water Res. **38:**1884–1892. http://dx.doi.org/10.1016/j.watres.2003.12.026.
6. **Sharma SK, Sebwato C, Petrusevski B, Schippers JC.** 2002. Effect of groundwater quality on adsorptive iron removal. J. Water Supply Res. Technol. **51:**199–208.
7. **Sharma SK, Petrusevski B, Schippers JC.** 2002. Characterisation of coated sand from iron removal plants. Water Supply **2:**247–258.
8. **Hu P-Y, Hsieh Y-H, Chen J-C, Chang C-Y.** 2004. Characteristics of manganese-coated sand using SEM and EDAX analysis. J. Colloid Interface Sci. **272:**308–313. http://dx.doi.org/10.1016/j.jcis.2003.12.058.

9. **Lo S-L.** 1996. Characteristics and adsorption properties of iron-coated sand. Water Sci. Technol. **35:**63–70.
10. **Buamah R, Petrusevski B, Schippers JC.** 2009. Oxidation of adsorbed ferrous iron: kinetics and influence of process conditions. Water Sci. Technol. **60:**2353–2363. http://dx.doi.org/10.2166/wst.2009.597.
11. **Mills AL, Herman JS, Hornberger GM, Dejesús H, Dejesus TH.** 1994. Effect of solution ionic strength and iron coatings on mineral grains on the sorption of bacterial cells to quartz sand. Appl. Environ. Microbiol. **60:** 3300–3306.
12. **Knapp EP, Herman JS, Hornberger GM, Mills AL.** 1998. The effect of distribution of iron-oxyhydroxide grain coatings on the transport of bacterial cells in porous media. Environ. Geol. **33:**243–248. http://dx.doi.org/10.1007/s002540050243.
13. **US Environmental Protection Agency.** 1996. Acid digestion of sediments, sludges, and soils: method 3050b. US Environmental Protection Agency, Washington, DC. http://www.epa.gov/osw/hazard/testmethods/sw846/pdfs/3050b.pdf.
14. **Tatari K, Smets BF, Albrechtsen H-J.** 2013. A novel bench-scale column assay to investigate site-specific nitrification biokinetics in biological rapid sand filters. Water Res. **47:**6380–6387. http://dx.doi.org/10.1016/j.watres.2013.08.005.
15. **Lee CO, Boe-Hansen R, Musovic S, Smets B, Albrechtsen H-J, Binning P.** 2014. Effects of dynamic operating conditions on nitrification in biological rapid sand filters for drinking water treatment. Water Res. **64:**226–236. http://dx.doi.org/10.1016/j.watres.2014.07.001.
16. **Pellicer-Nàcher C, Franck S, Gülay A, Ruscalleda M, Terada A, Al-Soud WA, Hansen MA, Sørensen SJ, Smets BF.** 2014. Sequentially aerated membrane biofilm reactors for autotrophic nitrogen removal: microbial community composition and dynamics. Microb. Biotechnol. **7:**32–43. http://dx.doi.org/10.1111/1751-7915.12079.
17. **Yu Y, Lee C, Kim J, Hwang S.** 2005. Group-specific primer and probe sets to detect methanogenic communities using quantitative real-time polymerase chain reaction. Biotechnol. Bioeng. **89:**670–679. http://dx.doi.org/10.1002/bit.20347.
18. **Pellicer-Nàcher C, Sun SP, Lackner S, Terada A, Schreiber F, Zhou Q, Smets BF.** 2010. Sequential aeration of membrane-aerated biofilm reactors for high-rate autotrophic nitrogen removal: experimental demonstration. Environ. Sci. Technol. **44:**7628–7634. http://dx.doi.org/10.1021/es1013467.
19. **Sundberg C, Al-Soud W a, Larsson M, Alm E, Yekta SS, Svensson BH, Sørensen SJ, Karlsson A.** 2013. 454 pyrosequencing analyses of bacterial and archaeal richness in 21 full-scale biogas digesters. FEMS Microbiol. Ecol. **85:**612–626. http://dx.doi.org/10.1111/1574-6941.12148.
20. **Sutton NB, Maphosa F, Morillo JA, Abu Al-Soud W, Langenhoff AA, Grotenhuis T, Rijnaarts HH, Smidt H.** 2013. Impact of long-term diesel contamination on soil microbial community structure. Appl. Environ. Microbiol. **79:**619–630. http://dx.doi.org/10.1128/AEM.02747-12.
21. **Caporaso JG, Kuczynski J, Stombaugh J, Bittinger K, Bushman FD, Costello EK, Fierer N, Peña AG, Goodrich JK, Gordon JI, Huttley GA, Kelley ST, Knights D, Koenig JE, Ley RE, Lozupone CA, Mcdonald D, Muegge BD, Pirrung M, Reeder J, Sevinsky JR, Turnbaugh PJ, Walters WA, Widmann J, Yatsunenko T, Zaneveld J, Knight R.** 2010. QIIME allows analysis of high-throughput community sequencing data. Nat. Methods **7:**335–336. http://dx.doi.org/10.1038/nmeth.f.303.
22. **Edgar RC, Haas BJ, Clemente JC, Quince C, Knight R.** 2011. UCHIME improves sensitivity and speed of chimera detection. Bioinformatics **27:** 2194–2200. http://dx.doi.org/10.1093/bioinformatics/btr381.
23. **DeSantis TZ, Hugenholtz P, Larsen N, Rojas M, Brodie EL, Keller K, Huber T, Dalevi D, Hu P, Andersen GL.** 2006. Greengenes, a chimera-checked 16S rRNA gene database and workbench compatible with ARB. Appl. Environ. Microbiol. **72:**5069–5072. http://dx.doi.org/10.1128/AEM.03006-05.
24. **Caporaso JG, Bittinger K, Bushman FD, DeSantis TZ, Andersen GL, Knight R.** 2010. PyNAST: a flexible tool for aligning sequences to a template alignment. Bioinformatics **26:**266–267. http://dx.doi.org/10.1093/bioinformatics/btp636.
25. **Altschul SF, Gish W, Miller W, Myers EW, Lipman DJ.** 1990. Basic local alignment search tool. J. Mol. Biol. **215:**403–410. http://dx.doi.org/10.1016/S0022-2836(05)80360-2.
26. **Pruesse E, Quast C, Knittel K, Fuchs BM, Ludwig W, Peplies J, Glöckner FO.** 2007. SILVA: a comprehensive online resource for quality checked and aligned ribosomal RNA sequence data compatible with ARB. Nucleic Acids Res. **35:**7188–7196. http://dx.doi.org/10.1093/nar/gkm864.
27. **Quast C, Pruesse E, Yilmaz P, Gerken J, Schweer T, Yarza P, Peplies J, Glockner FO.** 2013. The SILVA ribosomal RNA gene database project: improved data processing and web-based tools. Nucleic Acids Res. **41:** D590–D596. http://dx.doi.org/10.1093/nar/gks1219.
28. **Ludwig W, Strunk O, Westram R, Richter L, Meier H, Yadhukumar Buchner A, Lai T, Steppi S, Jobb G, Förster W, Brettske I, Gerber S, Ginhart AW, Gross O, Grumann S, Hermann S, Jost R, König A, Liss T, Lüssmann R, May M, Nonhoff B, Reichel B, Strehlow R, Stamatakis A, Stuckmann N, Vilbig A, Lenke M, Ludwig T, Bode A, Schleifer K-H.** 2004. ARB: a software environment for sequence data. Nucleic Acids Res. **32:**1363–1371. http://dx.doi.org/10.1093/nar/gkh293.
29. **Ferris MJ, Muyzer G, Mard DM.** 1996. Denaturing gradient gel electrophoresis profiles of 16S rRNA-defined populations inhabiting a hot spring microbial mat community. Appl. Environ. Microbiol. **62:**340–346.
30. **Rotthauwe JH, Witzel KP, Liesack W.** 1997. The ammonia monooxygenase structural gene *amoA* as a functional marker: molecular fine-scale analysis of natural ammonia-oxidizing populations. Appl. Environ. Microbiol. **63:**4704–4712.
31. **Francis CA, Roberts KJ, Beman JM, Santoro AE, Oakley BB.** 2005. Ubiquity and diversity of ammonia-oxidizing archaea in water columns and sediments of the ocean. Proc. Natl. Acad. Sci. U. S. A. **102:**14683–14688. http://dx.doi.org/10.1073/pnas.0506625102.
32. **Ririe KM, Rasmussen RP, Wittwer CT.** 1997. Product differentiation by analysis of DNA melting curves during the polymerase chain reaction. Anal. Biochem. **245:**154–160. http://dx.doi.org/10.1006/abio.1996.9916.
33. **Kinner NE, Harvey RW, Blakeslee K, Novarino G, Meeker LD.** 1998. Size-selective predation on groundwater bacteria by nanoflagellates in an organic-contaminated aquifer. Appl. Environ. Microbiol. **64:**618–625.
34. **Flemming H, Wingender J.** 2010. The biofilm matrix. Nat. Rev. Microbiol. **8:**623–633. http://dx.doi.org/10.1038/nrmicro2415.
35. **Prasad DY, Belsare DK.** 1984. The physico-chemical characteristics of the used filter sand and its role in the seven water works systems in a tropical region. Acta Hydrochim. Hydrobiol. **12:**73–80. http://dx.doi.org/10.1002/aheh.19840120113.
36. **Sharma SK.** 2001. Adsorptive iron removal from groundwater. Ph.D. thesis. Wageningen University, Wageningen, The Netherlands.
37. **Diz HR, Novak JT.** 1998. Fluidized bed for removing iron and acidity from acid mine drainage. J. Environ. Eng. **124:**701–708. http://dx.doi.org/10.1061/(ASCE)0733-9372(1998)124:8(701).
38. **Buamah R, Petrusevski B, Schippers JC.** 2008. Adsorptive removal of manganese(II) from the aqueous phase using iron oxide coated sand. J. Water Supply Res. Technol. **57:**1. http://dx.doi.org/10.2166/aqua.2008.078.
39. **Sahabi DM, Takeda M, Suzuki I, Koizumi J.** 2009. Removal of Mn^{2+} from water by "aged" biofilter media: the role of catalytic oxides layers. J. Biosci. Bioeng. **107:**151–157. http://dx.doi.org/10.1016/j.jbiosc.2008.10.013.
40. **Stahl DA, de la Torre JR.** 2012. Physiology and diversity of ammonia-oxidizing archaea. Annu. Rev. Microbiol. **66:**83–101. http://dx.doi.org/10.1146/annurev-micro-092611-150128.
41. **Martens-Habbena W, Berube PM, Urakawa H, de la Torre JR, Stahl DA.** 2009. Ammonia oxidation kinetics determine niche separation of nitrifying *Archaea* and *Bacteria*. Nature **461:**976–979. http://dx.doi.org/10.1038/nature08465.
42. **Schwartz T, Jungfer C, Heissler S, Friedrich F, Faubel W, Obst U.** 2009. Combined use of molecular biology taxonomy, Raman spectrometry, and ESEM imaging to study natural biofilms grown on filter materials at waterworks. Chemosphere **77:**249–257. http://dx.doi.org/10.1016/j.chemosphere.2009.07.002.
43. **White CP, Debry RW, Lytle DA.** 2012. Microbial survey of a full-scale, biologically active filter for treatment of drinking water. Appl. Environ. Microbiol. **78:**6390–6394. http://dx.doi.org/10.1128/AEM.00308-12.
44. **Chang Y, Li CW, Benjamin MM.** 1997. Iron oxide-coated media advantages over conventional sand media for NOM sorption and particulate filtration. Am. Water Works Assoc. J. **89:**100–113.
45. **Katsoyiannis I, Zouboulis A.** 2002. Removal of arsenic from contaminated water sources by sorption onto iron-oxide-coated polymeric materials. Water Res. **36:**5141–5155. http://dx.doi.org/10.1016/S0043-1354(02)00236-1.
46. **Lee CO.** 2014. Processes affecting nitrification performance in biological rapid sand filters. Ph.D thesis. Technical University of Denmark, Kgs. Lyngby, Denmark.